Article

Uncovering the Mechanism of the Hydrogen Poisoning on Ru Nanoparticles via Density Functional Theory Calculations

David S. Rivera Rocabado [1,*] , Mika Aizawa [1], Tomohiro G. Noguchi [2], Miho Yamauchi [2,3,4] and Takayoshi Ishimoto [1,*]

[1] Graduate School of Advanced Science and Engineering, Hiroshima University, 1-4-1 Kagamiyama, Higashi-Hiroshima, Hiroshima 739-8527, Japan; aizawa20@hiroshima-u.ac.jp
[2] International Institute for Carbon-Neutral Energy Research (WPI-I2CNER), Kyushu University, Motooka 744, Nishi-ku, Fukuoka 819-0395, Japan; noguchi@i2cner.kyushu-u.ac.jp (T.G.N.); yamauchi@i2cner.kyushu-u.ac.jp (M.Y.)
[3] Institute for Materials Chemistry and Engineering (IMCE), Motooka 744, Nishi-ku, Fukuoka 819-0395, Japan
[4] Advanced Institute for Materials Research (WPI-AIMR), Tohoku University, 2-1-1 Katahira, Aoba-ku, Sendai 980-8577, Japan
* Correspondence: davidsrr@hiroshima-u.ac.jp (D.S.R.R.); tishimo@hiroshima-u.ac.jp (T.I.); Tel.: +81-82-424-7726 (D.S.R.R.); +81-82-424-7739 (T.I.)

Abstract: Although hydrogen plays a crucial role in ammonia synthesis, very little is known about its poisoning of Ru catalysts. In this study, density functional theory calculations of H_2 and N_2 dissociations, and H atom binding on Ru_{153} were performed to provide a fundamental understanding of hydrogen poisoning. Because of the kinetic dominance of the H_2 dissociation over N_2 (vertically or horizontally adsorbed) splitting, the dissociated H atoms block the active sites required for horizontal (less energetically demanding dissociation) N_2 adsorption to occur either from the gas phase or after its geometrical transformation from being adsorbed vertically. Additionally, the dissociated H atoms withdraw electrons from the surface, which reduces the ability of the neighboring Ru atoms to donate electrons for N_2 activation, hindering its dissociation and suppressing ammonia synthesis.

Keywords: hydrogen poisoning; Ru nanoparticle; density functional theory; N_2/H_2 dissociation energy; N_2/H_2 activation energies; H atom binding energy

1. Introduction

Liquescent NH_3 is both a carbon-free fuel and hydrogen carrier, spurring the development of highly efficient ammonia synthesis (AS) catalysts. Most NH_3 is synthesized by the Haber–Bosch process, an energy-intensive process, as the AS reaction over iron-based catalysts takes brute force; more than 20 MPa of pressure and temperatures higher than 450 °C are required to achieve a practically interesting conversion [1,2]. Because of its high activity under mild conditions, the Ru catalyst is more suitable for green AS than Fe-based [1,3–5]. Thus, one of the strategies to decrease the energetic requirements of the Haber–Bosch process is replacing the Fe-based catalyst with Ru [1,3,4]. However, in the absence of basic promoters, the catalytic activity of Ru for AS is very little [6–10]. Generally, alkali or alkali earth promoters enhance the activity of the Ru catalyst via electron injection and, thus, lower the energy barrier for N_2 dissociation, the rate-determining step in AS [5,11]. Unfortunately, some of these promoters also stabilize H_2 adsorption; thus, the dissociated H and N atoms compete for the same sites leading to high surface coverage by H atoms, a process also known as hydrogen poisoning [11]. The negative H_2 reaction order for Ru nanoparticles suggests that the catalysts should operate at nonstoichiometric conditions, which are less thermodynamically favorable for the AS reaction [12,13]. Thus, a supported Ru catalyst that is less inhibited by hydrogen poisoning is highly desirable. Promoters such as Ba and La help against the inhibition effect of H_2 on the activity of Ru/MgO catalysts by

a faster intrinsic rate of N_2 dissociation and increasing the competition for active sites with adsorbed H atoms [5].

Similarly, the synergy of $C12A7e^-$ to reversibly store/release hydrogen and donate electrons to the Ru particles suppressed hydrogen poisoning and accelerated the cleavage of the N–N triple bond [14]. Another practical strategy to increase the catalyst's lifetime against H poisoning is alloying Ru, a catalyst that interacts weakly/strongly with N/H, and Fe, which interacts weakly/strongly with H/N [15]. The FeRu solid solution exhibited a positive H_2 reaction order, attributed to a reduced overlap of Ru *d*–states with the *s*–states from H compared to pristine Ru(0001) [15]. Theoretically, the H atom binding [15–17] and its diffusion [18,19] on Ru surfaces and the H_2 dissociative adsorption on Ru nanoparticles [20–22] were studied extensively. Modulation–excitation infrared spectroscopy (MEIRS) measurements together with density functional theory (DFT) calculations revealed that the dissociation of activated H_2 molecules is more probable than their adsorption, leading to the hydrogenation of the surface of the Ru catalyst [23]. Given the critical role of hydrogen in the AS reaction, little is known about the H poisoning mechanism. Theoretically, to model the vast intricateness of the effects, conditions, and their synergy during the reaction conditions, such as the adsorbate's coverage, the effect of the support, impurities, defects, the surface roughness of the support and nanoparticles, the size, shape, symmetry, and dispersion of the nanoparticles, the pre-treatment effect, the effect of pressure and temperature, etc., is impractical. Thus, theoretical researchers must find structures or models that are representative of the experimental conditions. Homogeneous surfaces or small clusters fail to explain the adsorption properties of real nanoparticles because, unlike ideal flat surfaces, nanoparticles feature a high degree of site heterogeneity, which depends on nanoparticle size and shape [23,24]. The Ru(0001) is the most stable surface orientation of the hexagonal close-packed Ru and has been widely used to study the H binding [15,16,24–28], N_2 adsorption [15,26,28–31], and NH_3 formation paths [15,16,32]. However, in the case of the AS, the activation of N_2 occurred only on Ru steps, which confirmed that the reaction is extremely sensitive to the structure of the Ru catalyst [16,25–27]. MEIRS measurements and DFT calculations exemplified the Ru(0001) limitation for the N_2 adsorption [23]. Under conditions similar to AS, the IR signal of N_2 adsorbed on Ru nanoparticles supported on MgO was deconvoluted into two major and several minor peaks [23]. DFT calculations of N_2 adsorption on Ru(0001) were only able to assign one of the largest peaks with considerable deviations from the experimental wavenumber [23]. Additionally, for the N_2 dissociation from its vertical interaction on flat [11] and stepped [13] Ru(0001), the horizontal N_2 adsorption appeared as a metastable molecularly adsorbed state. On the other hand, DFT calculations using a nanoparticle model containing 153 Ru atoms, Ru_{153}, were able to assign the multiplicity of N–N stretching modes to different vertical and horizontal N_2 adsorption configurations [23]. While some deviations were observed, the DFT-calculated and experimental wavenumbers were in good qualitative and semi-quantitative agreement to explain the multiple N_2/H_2 adsorption states and the source of the molecules' activation on Ru/MgO catalysts [23]. Moreover, DFT calculations of the H–H and H–Ru stretching modes from the H_2 and H atom interaction on Ru_{153}, respectively, showed excellent agreement with the experimental vibration frequencies [23]. For the reasons mentioned above, herein, DFT calculations of the H_2 and N_2 dissociations and H atom interactions on Ru_{153} were used to explain the mechanism of H poisoning on Ru catalysts. Our results show that H poisoning results from the barrierless H_2 dissociation. The dissociated H atoms physically and electronically hinder N_2 adsorption, activation, and dissociation, by which the AS is inhibited. These results are intended to illuminate the characteristics of H poisoning and help disrupt its effect on the activity of next-generation AS catalysts that are vital to establishing a viable carbon-free society.

2. Results

2.1. N_2 and H_2 Dissociation

2.1.1. N_2 Dissociation

The most stable configurations of N_2 adsorption on Ru_{153} were reported to be vertically on top of a vertex atom with an adsorption energy of -1.031 eV, and at a 4–fold (4F)–coordinated site with an adsorption energy of -1.021 eV [23]. From these two most stable configurations, the dissociation of the N_2 molecule has been studied, and all the stable structures are summarized in Figure S1 (top) and Figure S2 (4F). The N_2 dissociation energies from the top site range from -0.468 to -1.854 eV. The most stable configuration corresponds to each N atom binding to a 3–fold (3F)–coordinated site while sharing the same vertex atom. Both N atoms are charged negatively, -0.433 and -0.441 *e*, with average Ru–N bond orders of 0.970 and 0.938, respectively. Theoretically, electron donation from C12A7:O^{2-}, C12A7:O^{2-}/Ru_2, C12A7:e^-, and C12A7:e^-/Ru_2 to N atoms has also been reported [33], and it was hypothesized that electronic effects such as depletion of surface charge gives rise to a new hydrogen adsorption site and weakens the H_2 chemisorption state that exists on the bare surface [34]. The electron density difference for the dissociated N_2 on Ru_{153} is shown in Figure S3a. The energy barrier required to dissociate N_2 from its adsorption on top of a vertex atom to each N atom binding to a 3F site is approximately 1.96 eV, which is higher than our calculated energy barrier for the N_2 dissociation on Ru(0001), 1.49, and higher than the calculated energy required to split N_2 (0.66 eV) on Ru(10$\bar{1}$1) [35]. The transition state (TS) structure corresponding to the dissociation from the top site of Ru_{153} is one of the N atoms on top of the vertex atom, while the remaining N atom is on a bridge/3F site with a distance of 2.057 Å between the N atoms. The N_2 dissociation pathways from its most stable adsorption on the top site of Ru_{153}, vertically adsorbed on the top of a Ru atom of Ru(0001), and Ru(10$\bar{1}$1) [35] are represented in Figure 1a. The dissociation energies of N_2 from the 4F site range from -0.080 to -1.627 eV. After the N_2 adsorbs on a 4F site, the most stable dissociation leads to one of the N atoms binding to a 3F site and the other interacting on a bridge site. The N atoms for the most stable dissociated configuration are charged negatively, -0.404 and -0.392 *e*, with average Ru–N bond orders of 0.955 and 1.273 for the N atom binding on the 3F and bridge site, respectively. The electron density difference for the most stable N_2 dissociated from the 4F site of Ru_{153} is shown in Figure S3b. The dissociation of the N_2 horizontally adsorbed on the 4F has an energy barrier of 0.94 eV, which is higher than our calculated activation energy (0.81 eV) for the N_2 horizontally adsorbed on a 3F site of Ru(0001), and higher than the energy required (0.79 eV) to split the N_2 adsorbed horizontally on a 4F site of Ru(11$\bar{2}$1) [27]. For the N_2 dissociation from the most stable 4F site of Ru_{153}, the N–N distance at the TS is 1.902 Å, where each N atom is located at a bridge site. The difference in the energy barriers (1.02 eV) required to dissociate the N_2 from a top and 4F site arises from more electron donation from the four Ru atoms at the 4F site than a single atom at the top site [23]. Such charge transfer leads to a buildup of electron density at the N–N bond, destabilizing the N–N bond and activating the N_2 molecule [23]. These results prove the importance of the "side on" or horizontal adsorption of the N_2 to facilitate its dissociation (rate-determining step in AS) and speed up the reaction leading to the formation of NH_3. The dissociation reaction from N_2 interacting on the most stable 4F site of Ru_{153} is compared with the dissociation pathways of the N_2 horizontally adsorbed on Ru(0001), and Ru(11$\bar{2}$1) in Figure 1b.

2.1.2. H_2 Dissociation

The most stable configuration of the H_2 adsorption on Ru_{153} is horizontally on top of the same vertex atom as for the vertical N_2 interaction, with an adsorption energy of -0.655 eV [23]. The dissociation energies of the H_2 from such vertex sites range from -0.516 to -1.348 eV, as pictured in Figure S4. The configuration corresponding to the most stable H_2 dissociation is with each H atom interacting on a bridge site between a vertex and edge atom while sharing the same vertex atom. Similar to the negatively charged N atoms, the dissociated H atoms exhibit charges of -0.131 and -0.124 *e* and averaged Ru–H

bond orders of 0.540 and 0.560, respectively. The electron density difference for the most stable dissociated H_2 structure on Ru_{153} is depicted in Figure S5. Note that the most stable configurations of the H_2 dissociation are less exothermic than the N_2 dissociation, both from the N_2 vertically and horizontally adsorbed. Notice that the dissociated H atoms (Figure S4) interact with some of the same atoms as the dissociated N atoms shown in Figure S1. The energy barrier for the H_2 dissociation from the H_2 adsorbed on top of a vertex atom is 0.03 eV, which is the same for the H_2 dissociation on Ru(0001) and agrees with experimental observations of the spontaneous H_2 dissociation [36] and with MEIRS observations, suggesting that the dissociation of H_2 occurs immediately after the molecule's adsorption [23]. At the TS, the H atoms located on top of the vertex atom of Ru_{153} are separated 1.214 Å. The dissociation reaction from H_2 adsorbed on top of the most stable vertex atom is compared with the molecule's dissociation on Ru(0001) in Figure 2.
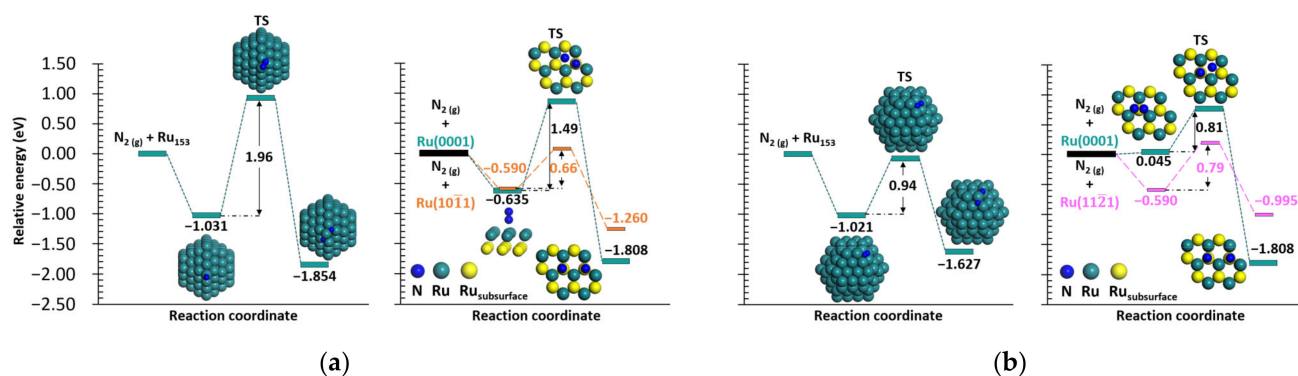

(a)   (b)

Figure 1. Calculated N_2 dissociation pathways (**a**) for the N_2 vertically adsorbed on the most stable top of a vertex atom of Ru_{153}, on the top sites of Ru(0001) and Ru(10$\bar{1}$1), (**b**) for the N_2 horizontally adsorbed on the most stable 4F site of Ru_{153}, on a 3F site of Ru(0001), and a 4F site of Ru(11$\bar{2}$1). Our calculated pathways for the N_2 dissociations on Ru_{153} and Ru(0001) are shown in turquoise blue together with their respective configurations of the adsorbed, TS, and dissociated N_2. Only the surface and subsurface Ru atoms are shown for the N_2 dissociation on Ru(0001). The pathways shown in orange and pink correspond only to the numeric values from references [27,35], respectively. The configurations corresponding to the adsorbed, TS, and dissociated N2 on the Ru(10$\bar{1}$1) and Ru(11$\bar{2}$1) can be found in references [27,35], respectively. The TS and energy barriers for the N_2 dissociation are also shown.
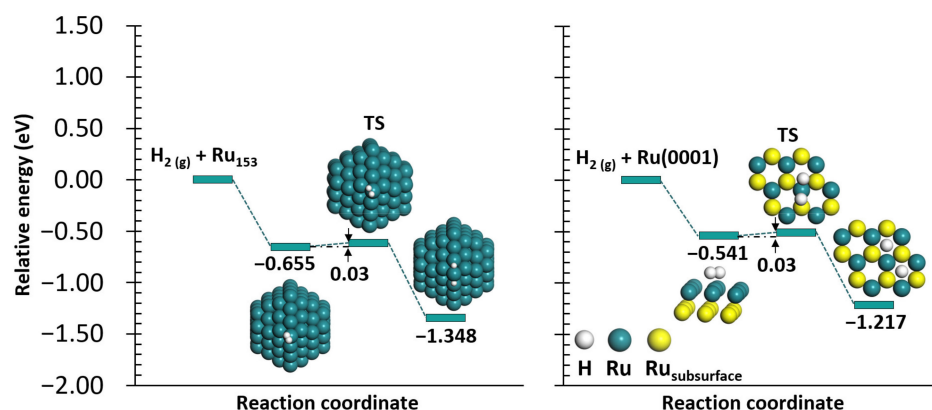

Figure 2. H_2 dissociation on Ru_{153} and Ru(0001). Only the surface and subsurface Ru atoms are shown for the H_2 dissociation on Ru(0001). The TS and energy barrier are also shown.

2.2. H Atom Binding

From exploring all the possible binding sites of the H atom on Ru_{153}, 25 symmetric adsorption sites were uncovered. The H atom interaction on the top of a vertex atom

(Figure S6) has a binding energy of -2.512 eV. Figure S7 summarizes the H atom binding on the bridge sites of Ru_{153} with binding energies ranging from -2.499 to -2.973 eV, from which the interaction of the H atom at the bridge site between two edge atoms is the most stable. The binding energies of the H atom interaction on the Ru_{153}'s 3F sites range from -2.751 to -2.913 eV, as shown in Figure S8. From all the stable configurations summarized in Figure S8, the most stable is for the H atom interacting with two edge atoms and one $\{10\bar{1}1\}$ facet atom. The binding energies of the H atom interaction on the 4F sites of Ru_{153} range from -2.554 to -2.770 eV, from which the most stable one is the H atom binding with two edge and two atoms of the $\{10\bar{1}1\}$ facet, as presented in Figure S9. Comparable to the H atoms from the H_2 dissociation, the Ru atoms donate electrons to the interacting H atom. It was reported that the H atom interacting on the threefold hollow site of Ru(0001) gains 0.051 e [37], which is in good agreement with our calculated value, 0.049 e (Figure S8), corresponding to the H atom interaction on the $\{0001\}$ facet of Ru_{153}. Although there is no clear relationship between the H binding energies and the charge of the H atom, for the most stable structures of the H atom binding on the top, bridge, 3F, and 4F sites, as the number of Ru atoms interacting with the adsorbate increases, the charge (in absolute values) decreases. On the other hand, the sum of the Ru–H bond order increases with increasing the number of Ru atoms interacting with the H atom. An approximate description of the H atom's s–orbital coupling with the s–, p–, and d–orbitals of the interacting Ru atoms at the top, bridge, 3F, and 4F sites is illustrated in Figure 3 using the projected crystal orbital Hamilton population (pCOHP) and the density of states (DOS) profiles.

　　Note that the DOS profiles of the Ru atoms at the adsorption site are averaged by the number of Ru atoms involved in the adsorption. Some dissimilarities exist between the DOS profiles of the individual Ru atoms of the most stable H binding on the 3F and 4F sites, and their averaged DOS profiles. These dissimilarities arise from the high degree of site heterogeneity arising from the unique features and properties (coordination number, charge, d-band center, etc.) of the symmetric atoms in Ru_{153}. The heterogeneity of the Ru_{153} surface sites is represented as heat maps of each Ru atom coordination number, charge, and d-band center elsewhere [23]. For the most stable structures of the H atom binding on the bridge, 3F, and 4F sites, the individual DOS profiles are compared to the averaged DOS in Figure S10. In this work, we use the averaged DOS profiles because it helps us explain the differences between the most stable structures of the H atom binding on top, bridge, 3F, and 4F sites. From the most stable H binding on the top, bridge, 3F, and 4F sites, the stability decreases in the following order: H atom interacting on the bridge, 3F, 4F, and top site. While some deviations arise from the difference in the size of the nanoparticle and its symmetry, the H atom binding energies reported here are in semi-quantitative and good qualitative agreement with DFT calculations of the H atom interaction on Ru_{55} [22]. On the other hand, theoretical [16,28] and experimental [38] works reported that the H atom thermodynamically favors the threefold hollow sites of Ru(0001), with binding energies of -2.98 [16] and -2.96 eV [28]. From the pCOHP and the DOS analyses, the most stable interaction of the H atom binding on the bridge site is dominated by the coupling of the Ru atoms' $5s$ and e_g orbitals with the $1s$ orbital from the H atom. Compared to the bridge interaction, the H atom binding on the top site is dominated by the combination of the Ru atom's $5p_y$, $4d_{xy}$, and the e_g orbitals, which are more upshifted compared to all the other adsorption sites. Additionally, the antibonding states are the most downshifted among all the most stable adsorption sites considered, helping to explain the weak binding on the top site. The difference in stability between the H interaction on 3F and 4F sites arises from the lower coupling of the Ru atoms' $4d_{xy}$, $4d_{yz}$, and $4d_{x^2-y^2}$ orbitals at the 4F site with the $1s$ from H atom. In Figure S11, the orbital combinations involved in the H–Ru interaction are decomposed for a more straightforward understanding.
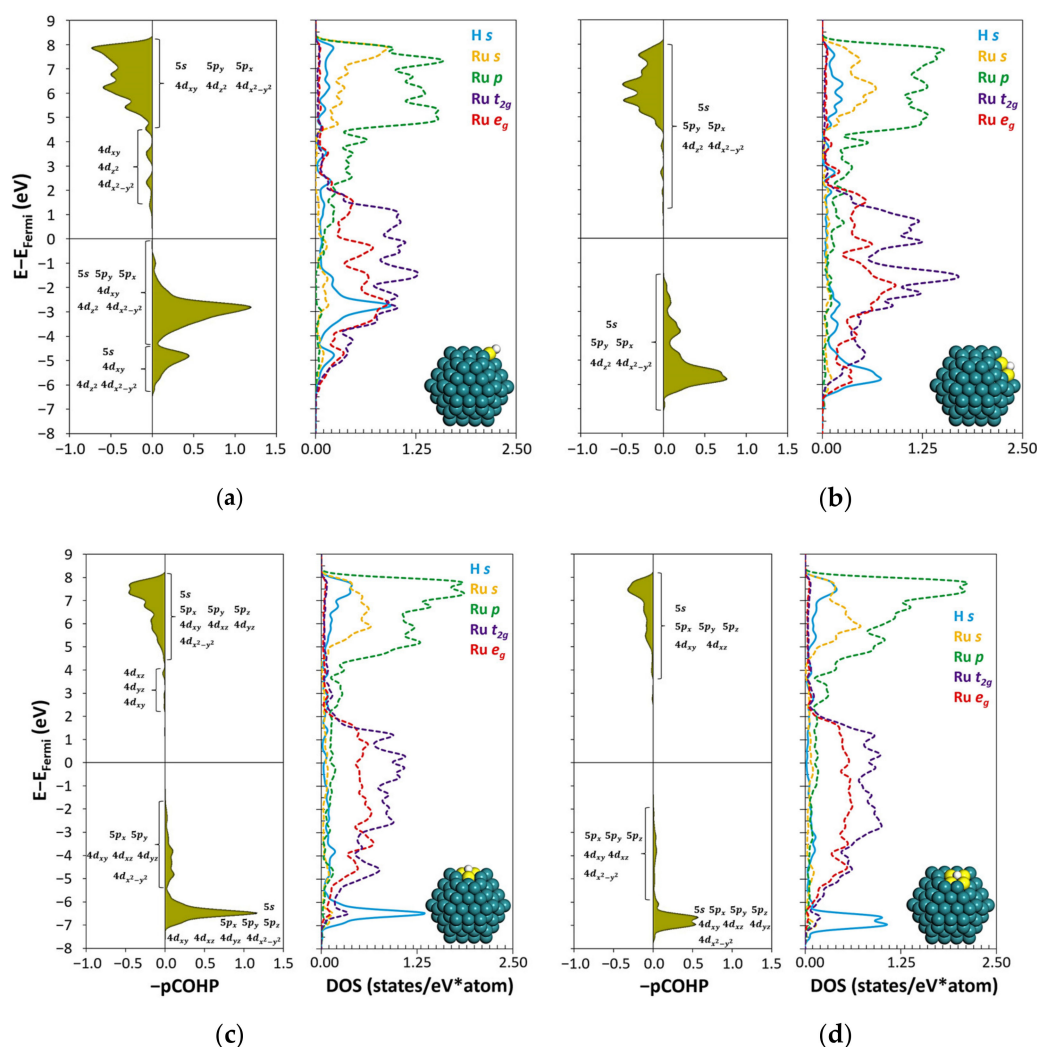
Figure 3. Bonding analyses of the H atom interacting on (**a**) top, (**b**) bridge, (**c**) 3F, and (**d**) 4F sites of Ru_{153}. The projected crystal orbital Hamilton population and the density of states of the H atom (white sphere) interacting with the Ru atoms (yellow spheres) are shown.

3. Discussion

From the reported H_2/N_2 adsorption states on Ru/MgO [23], there is a tendency that the N_2 adsorption is more stable than the H_2 when the adsorption site involves the same atoms (except for the vertical N_2 at the bridge site and N_2 horizontally on the top site). Although the difference in adsorption energies is sensitive to each of the adsorption sites in the nanoparticle, the more stable N_2 adsorption would be translated into N_2 molecules covering a large portion of the Ru nanoparticle. Additionally, DFT calculations [16] showed the more stable N atom interaction, -5.70 eV, compared to the binding energy of H atom, -2.98 eV on Ru(0001). For Ru(0001) pre-covered with N atoms, the presence of the N atoms inhibits H_2 adsorption [16], and it was hypothesized that as the concentration of N atoms on the surface increases, the depletion of the surface charge leads to a new hydrogen adsorption site [34]. Thus, H_2 must dissociate quickly before N_2 adsorption for H atom poisoning to occur. Such affirmation agrees with our calculated activation energy of 0.03 eV and MEIRS observations where H_2 and H atom peaks were observed on Ru/MgO [23]. It is even probable that the dissociated H atoms could hinder further H_2 adsorption and its dissociation as suggested by the time-domain IR spectrum where the peak corresponding to H_2 adsorption on Ru/MgO decreased with time and the one corresponding to H atom binding did not vary significantly, suggesting that the hydrogenation of the Ru nanoparticle

proceeds with time [23]. When gas phase H_2 approaches the surface of the Ru_{153} to interact vertically with the nanoparticle's adsorption sites, the molecule either adsorbs physically at distances between 3.313–3.652 Å or rotates to chemisorb horizontally as previously reported [23]. These results suggest that the H_2 orientation is important and that horizontal interaction is required for the activation of H_2 before its non-activated dissociation. Although the dissociated H atoms and the N_2 molecules compete for the same adsorption sites, some N_2 molecules could adsorb vertically on top of the Ru atoms as the dissociated H atoms prefer to bind to bridge, 3F, and 4F sites before the top sites, as shown in Figure S4 and from the interaction of an H atom on Ru_{153} (Figures S6–S9). The effect of H_2 on the isotopic equilibration of N_2 on various Ru catalysts showed that the fraction of adsorption sites occupied by H atoms was ca. 5:1 compared to adsorbed N atoms [39]. A kinetic model revealed that the H atoms coverage is 46 times larger than the coverage of the N atoms [5]. While adsorbed N and H atoms retard N_2 activation over different Ru catalysts, the main retarding species are the adsorbed H atoms [40].

Similarly, there is a lower probability of horizontal N_2 adsorption either from the gas phase or after its rotation and diffusion from its vertical interaction because of the stable H atom binding preferences. To corroborate this statement, Figure S12 summarizes the possible H_2 dissociated configurations where the H atoms block one of the adsorption sites required for horizontal N_2 adsorption at the 4F site. Obstructing N_2 horizontal adsorption translates to a lower NH_3 production rate because of the higher energy barrier required to split the N_2 vertically adsorbed (1.96 eV) compared to the horizontal configuration (0.94 eV). Figures S1 and S2 summarize the stable configurations of the N_2 dissociation from the top and 4F sites, respectively, and Figures S4 and S12 show the stable configurations of dissociated H atoms that are occupying at least one of the same binding sites required for the N_2 dissociation. These results can explain why the activity of Ru catalysts in the absence of basic promoters is minimal [6–10], and the necessity of such promoters to improve the activity of the Ru catalyst via a trade-off effect between a faster N_2 dissociation and greater competition for the active sites with H atoms [5].

Besides the physical obstruction of the active sites for N_2 adsorption, activation, and dissociation, from the electron density difference and charge analyses (Figure S5), the dissociated H atoms withdraw and localize electron density from the Ru nanoparticle. It has been shown that N_2 activation occurs from electron density accumulation between the N–N bonds due to electron donation from the Ru atoms to the N_2 molecule [23]. Thus, as the Ru atoms donate electrons to stabilize the dissociated H atoms, the surface Ru atoms will be less capable of donating electrons for the activation of N_2, further dissociation, and stabilizing the dissociated N atoms that also withdraw and localize electron density. Following the hypothesis that the increased concentration of chemisorbed N atoms leads to a depletion of the surface charge [16], then H atoms present on the catalyst's surface would decrease the electron donation ability of the surface Ru atoms since both N and H atoms withdraw electrons. However, more calculations are required to understand the co-adsorption of N_2 and dissociated H atoms and their hindering effect on N_2 adsorption and activation. Additionally, the presence of preabsorbed atoms or molecules that can exhibit repulsive forces with the incoming H_2 molecules to prevent the spontaneous H_2 dissociation should also be addressed to avoid H atom poisoning.

4. Computational Methods

All calculations were based on the plane-wave DFT method implemented in the Vienna ab initio simulation package (VASP 5.6.2) [41–43]. Perdew−Burke−Ernzerhof parametrization under the generalized gradient approximation was employed as the exchange–correlation functional together with the projector-augmented wave method [44]. Spin-polarized calculations were performed throughout the study with a plane-wave cutoff energy of 600 eV. The convergence criterion for the geometry optimization calculations was set as the point at which the difference in the total energy between the two ionic steps was less than 10^{-5} eV/atom. Such energy optimization criterion led to atomic forces of up to

0.003 eV/Å for the optimization of the nanoparticle. For the self-consistent-field iterations, a criterion of 10^{-6} eV/atom was considered. The optimization of the HCP structure of the 1.58 nm diameter Ru nanoparticle, Ru_{153}, was performed at the Γ point in reciprocal space owing to the significant spatial extent of the system, where all Ru atoms were allowed to relax. The distance between neighboring image Ru nanoparticles was set as 15 Å to avoid interaction between periodic images, as shown in Figure 4a. The nanoparticle model comprises two facets, {0001} and {10$\bar{1}$1}, 18 atoms located at vertices, and 42 atoms located at ridges, as illustrated in Figure 4b. We have previously investigated H_2 and N_2 adsorption on the 12 symmetric adsorption sites and their possible combinations on Ru_{153} [23]. In this work, the dissociation energies of the most stable adsorbed N_2 and H_2 configurations are estimated. Additionally, the H atom binding to Ru_{153} is described to complement the results of the H atom interaction only on the 12 symmetric sites of Ru_{153} [23].
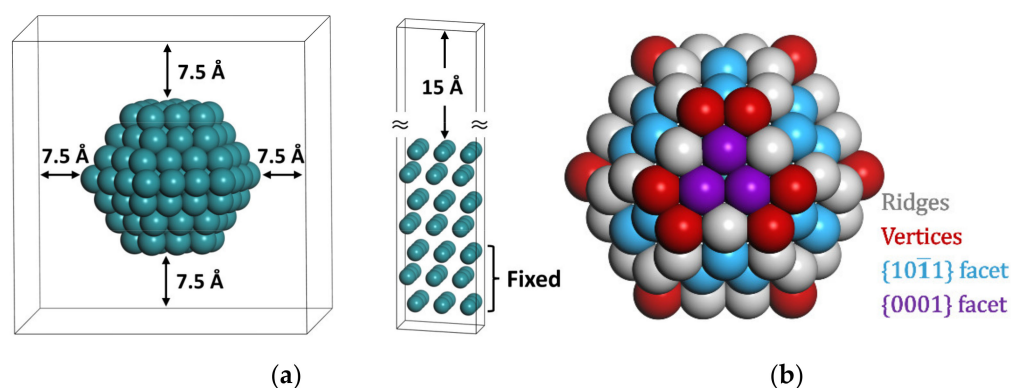

Figure 4. (**a**) Models of the Ru_{153} nanoparticle and Ru(0001) and (**b**) distribution of Ru atoms at facets, ridges, and vertices.

The N_2 and H_2 dissociation reactions on Ru(0001) were calculated on a 3×3 supercell containing seven atomic Ru layers. As shown in Figure 4a, the vacuum between the slabs was set to span a range of 15 Å to ensure no significant interaction between the slabs. The optimization was performed with a $4 \times 4 \times 1$ Monkhorst−Pack k-point mesh for the Brillouin zone integration where the atoms of the bottom three layers were kept fixed, and those of the top four layers were allowed to relax. The convergence criterion for the geometry optimization calculations was set as the point at which the atomic forces were lower than 0.005 eV/Å. For the self-consistent-field iterations, a criterion of 10^{-5} eV/atom was considered. The energies of N_2 and H_2 adsorption on Ru(0001) (E_{ads}), the energies for the dissociation of the molecules on Ru_{153} and Ru(0001) (E_{dis}), and the H binding on Ru nanoparticles (E_{bin}) were calculated as:

$$E_{ads/dis/bin} = E_{Ru_{n/s}+adsorbate} - E_{Ru_{n/s}} - E_{adsorbate}, \tag{1}$$

where $E_{Ru_{n/s}+adsorbate}$, $E_{Ru_{n/s}}$, and $E_{adsorbate}$ denote the total energies of N_2, H_2, or H atoms interacting with the Ru nanoparticle or N_2, H_2 interacting with Ru(0001), the total energy of an isolated Ru nanoparticle or pristine Ru(0001), and the total energies of isolated N_2, H_2, and an H atom, respectively. According to this definition, negative adsorption/dissociation/binding energies denote more stable adsorbate–Ru interactions. While all atoms were relaxed during the optimization of the H_2, N_2 dissociations, and the H atom binding to Ru_{153}, only the adsorbate and the Ru atoms in the top four layers were allowed to relax for H_2 and N_2 adsorption/dissociation on Ru(0001). After the geometrical optimization of the adsorbate interaction on Ru_{153}, the atomic forces were no greater than 0.020, 0.009, and 0.009 eV/Å for the N_2 and H_2 dissociation and the H atom interaction on Ru_{153}, respectively. Because of the significant size of the system, no dipole correction was considered for the adsorbate-induced dipole. Bond order and charge analyses were performed using the sixth-generation density-derived electrostatic and chemical method [45].

The energy barriers for N_2 and H_2 dissociations on Ru_{153} and $Ru(0001)$ were calculated by employing the climbing image nudged elastic band (CI–NEB) method [46,47]. Five linearly interpolated images were generated as intermediate structures between the most stable H_2/N_2 adsorption and dissociation structures. A spring constant of -5 eV/Å^2 was used to maintain the spacing between adjacent images. Because of the large size of the adsorbate-Ru_{153} system, during the NEB calculations, all atoms were allowed to relax until the atomic forces were lower than 0.3 eV/Å. Tighter force convergence criteria (0.05 eV/Å) showed that the calculated energy barrier for H_2 dissociation is converged within 10^{-4} eV/Å. On the other hand, the TS search calculations for N_2 and H_2 dissociations on $Ru(0001)$ were performed until the atomic forces of the adsorbate and the Ru atoms in the top four layers were lower than 0.03 eV/Å. After the convergence of the NEB calculations, the highest-energy structure obtained from the five images is the TS. To corroborate that the structures indeed correspond to the TSs of the N_2, and H_2 dissociations on Ru_{153} and $Ru(0001)$, vibrational calculations were performed using central differences with atomic displacements of ± 0.015 Å in all three Cartesian directions. The construction of the dynamical matrix was carried out by simply displacing the N and H atoms in the transition states structures corresponding to N_2 and H_2 dissociation. The self-consistent-field iterations convergence criterion was set to 10^{-8} eV/atom for all the vibrational calculations. By calculating the vibrational frequencies, we confirmed that the obtained transition states have one imaginary frequency, thus, validating the TS structures obtained. The bonding analyses corresponding to the H atom interaction on the active sites of Ru_{153} were performed using the pCOHP and DOS profiles obtained using the local-orbital basis suite towards electronic-structure reconstruction program [48–51].

5. Conclusions

To elucidate the mechanism of hydrogen poisoning of Ru catalysts, the N_2/H_2 dissociations and the H atom interaction were investigated on a Ru nanoparticle model and compared to the N_2/H_2 dissociation pathways on $Ru(0001)$ using DFT calculations. Additionally, the energetics of the N_2 dissociation were compared to two stepped surfaces from the literature, $Ru(10\bar{1}1)$ [35] and $Ru(11\bar{2}1)$ [27]. Except for the horizontal N_2 adsorption on $Ru(0001)$, the vertical and horizontal N_2 adsorption and dissociation are more thermodynamically stable on Ru_{153}, followed by the planar $Ru(0001)$, and the stepped surfaces. The opposite trend is observed for the energy barrier required to dissociate the N_2; stepped Ru surfaces, followed by the $Ru(0001)$, and then Ru_{153}. H_2 adsorbs and dissociates more stably on Ru_{153} than on $Ru(0001)$. However, for both Ru_{153} and $Ru(0001)$, the energy barrier to dissociate H_2 is almost zero. Because of the barrierless H_2 dissociation, the poisoning of the Ru catalyst can occur via (i) physical blocking of the surface sites, where the dissociated H atoms block the surface Ru atoms needed for N_2 vertical and horizontal adsorption. Compared to vertical N_2 adsorption, the dissociation of horizontal N_2 is less energetically demanding by 1.02 eV. However, the presence of dissociated H atoms will hinder horizontal N_2 adsorption from the gas phase or, after its geometrical transformation, from being adsorbed vertically. Additionally, from the dissociated N_2 and H_2 configurations, both N and H atoms prefer the same sites; hence, N_2 dissociation is stalled. (ii) Reducing the ability of neighboring Ru atoms to donate electrons to activate the adsorbed N_2 molecules in the vicinity of the dissociated H atoms. In this way, the catalytic activity of Ru toward N_2 dissociation and, henceforth, the AS, is suppressed.

the DOS profiles of the individual Ru atoms and their average DOS for the most stable structures of the H atom binding on bridge, 3F, and 4F sites, Figure S11: Atomic orbital decomposition of the H atom binding on the most stable top, bridge, 3F, and 4F sites of Ru153, Figure S12: Dissociated H atoms on the same sites required for the N2 adsorption and dissociation from the 4F site, and Figure S13: Interatomic Ru-Ru distances of surface atoms of Ru153 and HCP bulk Ru.

Author Contributions: Conceptualization, D.S.R.R., T.G.N., M.Y. and T.I.; methodology, D.S.R.R., T.G.N., M.Y. and T.I.; validation, D.S.R.R. and M.A.; formal analysis, D.S.R.R. and M.A.; investigation, D.S.R.R. and T.G.N.; resources, M.Y. and T.I.; data curation, D.S.R.R. and M.A.; writing—original draft preparation, D.S.R.R., M.A., T.G.N., M.Y. and T.I.; writing—review and editing, D.S.R.R., M.A., T.G.N., M.Y. and T.I.; visualization, D.S.R.R.; supervision, M.Y. and T.I.; project administration, M.Y. and T.I.; funding acquisition, M.Y. and T.I. All authors have read and agreed to the published version of the manuscript.

Data Availability Statement: All relevant data are included in the paper or the supporting information.

Conflicts of Interest: The authors declare no conflict of interest. The funders had no role in the design of the study; in the collection, analyses, or interpretation of data; in the writing of the manuscript, or in the decision to publish the results.

References

1. Ogura, Y.; Sato, K.; Miyahara, S.; Kawano, Y.; Toriyama, T.; Yamamoto, T.; Matsumura, S.; Hosokawa, S.; Nagaoka, K. Efficient ammonia synthesis over a Ru/La$_{0.5}$Ce$_{0.5}$O$_{1.75}$ catalyst pre-reduced at high temperature. *Chem. Sci.* **2018**, *9*, 2230–2237. [CrossRef] [PubMed]
2. Valera-Medina, A.; Amer-Hatem, F.; Azad, A.K.; Dedoussi, I.C.; de Joannon, M.; Fernandes, R.X.; Glarborg, P.; Hashemi, H.; He, X.; Mashruk, S.; et al. Review on Ammonia as a Potential Fuel: From Synthesis to Economics. *Energy Fuels* **2021**, *35*, 6964–7029. [CrossRef]
3. Sato, K.; Imamura, K.; Kawano, Y.; Miyahara, S.; Yamamoto, T.; Matsumura, S.; Nagaoka, K. A low-crystalline ruthenium nano-layer supported on praseodymium oxide as an active catalyst for ammonia synthesis. *Chem. Sci.* **2017**, *8*, 674–679. [CrossRef] [PubMed]
4. Sato, K.; Miyahara, S.; Ogura, Y.; Tsujimaru, K.; Wada, Y.; Toriyama, T.; Yamamoto, T.; Matsumura, S.; Nagaoka, K. Surface Dynamics for Creating Highly Active Ru Sites for Ammonia Synthesis: Accumulation of a Low-Crystalline, Oxygen-Deficient Nanofraction. *ACS Sustain. Chem. Eng.* **2020**, *8*, 2726–2734. [CrossRef]
5. Siporin, S.; Davis, R. Use of kinetic models to explore the role of base promoters on Ru/MgO ammonia synthesis catalysts. *J. Catal.* **2004**, *225*, 359–368. [CrossRef]
6. Murata, S. Preparation and characterization of chlorine-free ruthenium catalysts and the promoter effect in ammonia synthesis: 2. A lanthanide oxide-promoted Ru/Al$_2$O$_3$ catalyst. *J. Catal.* **1992**, *136*, 118–125. [CrossRef]
7. Aika, K.; Kumasaka, M.; Oma, T.; Kato, O.; Matsuda, H.; Watanabe, N.; Yamazaki, K.; Ozaki, A.; Onishi, T. Support and promoter effect of ruthenium catalyst. III. Kinetics of ammonia synthesis over various Ru catalysts. *Appl. Catal.* **1986**, *28*, 57–68. [CrossRef]
8. Aika, K. Preparation and characterization of chlorine-free ruthenium catalysts and the promoter effect in ammonia synthesis: 3. A magnesia-supported ruthenium catalyst. *J. Catal.* **1992**, *136*, 126–140. [CrossRef]
9. Szmigiel, D.; Bielawa, H.; Kurtz, M.; Hinrichsen, O.; Muhler, M.; Raróg, W.; Jodzis, S.; Kowalczyk, Z.; Znak, L.; Zieliński, J. The Kinetics of Ammonia Synthesis over Ruthenium-Based Catalysts: The Role of Barium and Cesium. *J. Catal.* **2002**, *205*, 205–212. [CrossRef]
10. Raróg, W.; Kowalczyk, Z.; Sentek, J.; Składanowski, D.; Zieliński, J. Effect of K, Cs and Ba on the kinetics of NH$_3$ synthesis over carbon-based ruthenium catalysts. *Catal. Lett.* **2000**, *68*, 163–168. [CrossRef]
11. Kitano, M.; Inoue, Y.; Ishikawa, H.; Yamagata, K.; Nakao, T.; Tada, T.; Matsuishi, S.; Yokoyama, T.; Hara, M.; Hosono, H. Essential role of hydride ion in ruthenium-based ammonia synthesis catalysts. *Chem. Sci.* **2016**, *7*, 4036–4043. [CrossRef]
12. Üner, D.; Aslan, M.Y. Using spilled over hydrogen in NH$_3$ synthesis over supported Ru catalysts. *Catal. Today* **2016**, *272*, 49–57. [CrossRef]
13. Rosowski, F.; Hornung, A.; Hinrichsen, O.; Herein, D.; Muhler, M.; Ertl, G. Ruthenium catalysts for ammonia synthesis at high pressures: Preparation, characterization, and power-law kinetics. *Appl. Catal. A Gen.* **1997**, *151*, 443–460. [CrossRef]
14. Hara, M.; Kitano, M.; Hosono, H. Ru-Loaded C12A7:e$^-$ Electrode as a Catalyst for Ammonia Synthesis. *ACS Catal.* **2017**, *7*, 2313–2324. [CrossRef]

15. Ghuman, K.K.; Tozaki, K.; Sadakiyo, M.; Kitano, S.; Oyabe, T.; Yamauchi, M. Tailoring widely used ammonia synthesis catalysts for H and N poisoning resistance. *Phys. Chem. Chem. Phys.* **2019**, *21*, 5117–5122. [CrossRef]

16. Zhang, C.J.; Lynch, M.; Hu, P. A density functional theory study of stepwise addition reactions in ammonia synthesis on Ru(0001). *Surf. Sci.* **2002**, *496*, 221–230. [CrossRef]

17. Truflandier, L.A.; Del Rosal, I.; Chaudret, B.; Poteau, R.; Gerber, I.C. Where does Hydrogen Adsorb on Ru Nanoparticles? A Powerful Joint ^{2}H MAS-NMR/DFT Approach. *ChemPhysChem* **2009**, *10*, 2939–2942. [CrossRef]

18. Mak, C.H.; George, S.M. Surface diffusion of hydrogen on Ru(001): Transition state theory calculations. *Chem. Phys. Lett.* **1987**, *135*, 381–386. [CrossRef]

19. Kristinsdóttir, L.; Skúlason, E. A systematic DFT study of hydrogen diffusion on transition metal surfaces. *Surf. Sci.* **2012**, *606*, 1400–1404. [CrossRef]

20. Del Rosal, I.; Mercy, M.; Gerber, I.C.; Poteau, R. Ligand-Field Theory-Based Analysis of the Adsorption Properties of Ruthenium Nanoparticles. *ACS Nano* **2013**, *7*, 9823–9835. [CrossRef]

21. Ge, G.-X.; Yan, H.-X.; Jing, Q.; Luo, Y.-H. Theoretical Study of Hydrogen Adsorption on Ruthenium Clusters. *J. Clust. Sci.* **2011**, *22*, 473–489. [CrossRef]

22. Cusinato, L.; Martínez-Prieto, L.M.; Chaudret, B.; del Rosal, I.; Poteau, R. Theoretical characterization of the surface composition of ruthenium nanoparticles in equilibrium with syngas. *Nanoscale* **2016**, *8*, 10974–10992. [CrossRef] [PubMed]

23. Rivera Rocabado, D.S.; Noguchi, T.G.; Hayashi, S.; Maeda, N.; Yamauchi, M.; Ishimoto, T. Adsorption States of N_2/H_2 Activated on Ru Nanoparticles Uncovered by Modulation–Excitation Infrared Spectroscopy and Density Functional Theory Calculations. *ACS Nano* **2021**, *15*, 20079–20086. [CrossRef]

24. Dean, J.; Taylor, M.G.; Mpourmpakis, G. Unfolding Adsorption on Metal Nanoparticles: Connecting Stability with Catalysis. *Sci. Adv.* **2019**, *5*, eaax5101. [CrossRef]

25. Dahl, S.; Tornqvist, E.; Chorkendorff, I. Dissociative Adsorption of N_2 on Ru: A Surface Reaction Totally Dominated by Steps. *J. Catal.* **2000**, *192*, 381–390. [CrossRef]

26. Dahl, S.; Logadottir, A.; Egeberg, R.C.; Larsen, J.H.; Chorkendorff, I.; Törnqvist, E.; Nørskov, J.K. Role of Steps in N_2 Activation on Ru(0001). *Phys. Rev. Lett.* **1999**, *83*, 1814–1817. [CrossRef]

27. Shetty, S.; Jansen, A.P.J.; van Santen, R.A. Active Sites for N_2 Dissociation on Ruthenium. *J. Phys. Chem. C* **2008**, *112*, 17768–17771. [CrossRef]

28. Herron, J.A.; Tonelli, S.; Mavrikakis, M. Atomic and Molecular Adsorption on Ru(0001). *Surf. Sci.* **2013**, *614*, 64–74. [CrossRef]

29. Mortensen, J.J.; Morikawa, Y.; Hammer, B.; Nørskov, J.K. Density Functional Calculations of N_2 Adsorption and Dissociation on a Ru(0001) Surface. *J. Catal.* **1997**, *169*, 85–92. [CrossRef]

30. De Paola, R.A.; Hoffmann, F.M.; Heskett, D.; Plummer, E.W. Adsorption of Molecular Nitrogen on Clean and Modified Ru(001) Surfaces: The Role of σ Bonding. *Phys. Rev. B Condens. Matter* **1987**, *35*, 4236–4249. [CrossRef]

31. Anton, A.B.; Avery, N.R.; Toby, B.H.; Weinberg, W.H. The Chemisorption of Nitrogen on the (001) Surface of Ruthenium. *J. Electron Spectros. Relat. Phenomena* **1983**, *29*, 181–186. [CrossRef]

32. Ishikawa, A.; Doi, T.; Nakai, H. Catalytic Performance of Ru, Os, and Rh Nanoparticles for Ammonia Synthesis: A Density Functional Theory Analysis. *J. Catal.* **2018**, *357*, 213–222. [CrossRef]

33. Kuganathan, N.; Hosono, H.; Shluger, A.L.; Sushko, P.V. Enhanced N_2 Dissociation on Ru-Loaded Inorganic Electride. *J. Am. Chem. Soc.* **2014**, *136*, 2216–2219. [CrossRef] [PubMed]

34. Seets, D.C.; Wheeler, M.C.; Mullins, C.B. Thermal desorption of hydrogen from atomic nitrogen precovered Ru(001). *J. Chem. Phys.* **1995**, *103*, 10399–10400. [CrossRef]

35. Casey-Stevens, C.A.; Lambie, S.G.; Ruffman, C.; Skúlason, E.; Garden, A.L. Geometric and Electronic Effects Contributing to N_2 Dissociation Barriers on a Range of Active Sites on Ru Nanoparticles. *J. Phys. Chem. C* **2019**, *123*, 30458–30466. [CrossRef]

36. Pozzo, M.; Alfè, D. Hydrogen dissociation and diffusion on transition metal (=Ti, Zr, V, Fe, Ru, Co, Rh, Ni, Pd, Cu, Ag)-doped Mg(0001) surfaces. *Int. J. Hydrogen Energy* **2009**, *34*, 1922–1930. [CrossRef]

37. Onwudinanti, C.; Tranca, I.; Morgan, T.; Tao, S. Tin, The Enabler—Hydrogen Diffusion into Ruthenium. *Nanomaterials* **2019**, *9*, 129. [CrossRef]

38. Thiel, P.A.; Weinberg, W.H. Adsite symmetry and vibrational structure of NO and H_2 co-adsorbed on the Ru(001) surface. *J. Chem. Phys.* **1980**, *73*, 4081–4085. [CrossRef]

39. Urabe, K. Activation of nitrogen by alkali metal-promoted transition metal VI. Hydrogen effect on isotopic equilibration of nitrogen and rate-determining step of ammonia synthesis on potassium-promoted ruthenium catalysts. *J. Catal.* **1976**, *42*, 197–204. [CrossRef]

40. Aika, K. Role of alkali promoter in ammonia synthesis over ruthenium catalysts—Effect on reaction mechanism. *Catal. Today* **2017**, *286*, 14–20. [CrossRef]

41. Kresse, G.; Hafner, J. Ab initio molecular dynamics for liquid metals. *Phys. Rev. B* **1993**, *47*, 558–561. [CrossRef] [PubMed]

42. Kresse, G.; Furthmüller, J. Efficient iterative schemes for ab initio total-energy calculations using a plane-wave basis set. *Phys. Rev. B—Condens. Matter Mater. Phys.* **1996**, *54*, 11169–11186. [CrossRef] [PubMed]

43. Kresse, G.; Furthmüller, J. Efficiency of ab-initio total energy calculations for metals and semiconductors using a plane-wave basis set. *Comput. Mater. Sci.* **1996**, *6*, 15–50. [CrossRef]

44. Blöchl, P.E. Projector augmented-wave method. *Phys. Rev. B* **1994**, *50*, 17953–17979. [CrossRef]

45. Manz, T.A. Introducing DDEC6 atomic population analysis: Part 3. Comprehensive method to compute bond orders. *RSC Adv.* **2017**, *7*, 45552–45581. [CrossRef]
46. Henkelman, G.; Uberuaga, B.P.; Jónsson, H. A climbing image nudged elastic band method for finding saddle points and minimum energy paths. *J. Chem. Phys.* **2000**, *113*, 9901–9904. [CrossRef]
47. Henkelman, G.; Jónsson, H. Improved tangent estimate in the nudged elastic band method for finding minimum energy paths and saddle points. *J. Chem. Phys.* **2000**, *113*, 9978–9985. [CrossRef]
48. Dronskowski, R.; Bloechl, P.E. Crystal orbital Hamilton populations (COHP): Energy-resolved visualization of chemical bonding in solids based on density-functional calculations. *J. Phys. Chem.* **1993**, *97*, 8617–8624. [CrossRef]
49. Deringer, V.L.; Tchougréeff, A.L.; Dronskowski, R. Crystal Orbital Hamilton Population (COHP) Analysis as Projected from Plane-Wave Basis Sets. *J. Phys. Chem. A* **2011**, *115*, 5461–5466. [CrossRef]
50. Maintz, S.; Deringer, V.L.; Tchougréeff, A.L.; Dronskowski, R. Analytic projection from plane-wave and PAW wavefunctions and application to chemical-bonding analysis in solids. *J. Comput. Chem.* **2013**, *34*, 2557–2567. [CrossRef]
51. Maintz, S.; Deringer, V.L.; Tchougréeff, A.L.; Dronskowski, R. LOBSTER: A tool to extract chemical bonding from plane-wave based DFT. *J. Comput. Chem.* **2016**, *37*, 1030–1035. [CrossRef]